Taylor & Francis
Taylor & Francis Group

Mechanics Based Design of Structures and Machines

An International Journal

ISSN: (Print) (Online) Journal homepage: https://www.tandfonline.com/loi/lmbd20

An investigation of the crashworthiness performance and optimization of tetra-chiral and reentrant crash boxes

Cüneyt Aktaş, Erdem Acar, Mehmet Ali Güler & Murat Altın

To cite this article: Cüneyt Aktaş, Erdem Acar, Mehmet Ali Güler & Murat Altın (2022): An investigation of the crashworthiness performance and optimization of tetra-chiral and reentrant crash boxes, Mechanics Based Design of Structures and Machines, DOI: 10.1080/15397734.2022.2075382

To link to this article: https://doi.org/10.1080/15397734.2022.2075382

MECHANICS BASED DESIGN OF STRUCTURES AND MACHINES
https://doi.org/10.1080/15397734.2022.2075382

An investigation of the crashworthiness performance and optimization of tetra-chiral and reentrant crash boxes

Cüneyt Aktaş[a], Erdem Acar[a], Mehmet Ali Güler[b], and Murat Altın[c]

[a]Department of Mechanical Engineering, TOBB University of Economics and Technology, Ankara, Turkey;
[b]College of Engineering and Technology, American University of the Middle East, Kuwait City, Kuwait;
[c]Department of Automotive Engineering, Gazi Üniversity, Ankara, Turkey

ABSTRACT

In this study, the crash performances of square and cylindrical crash boxes with tetra-chiral and reentrant unit cell structures were explored and optimized. First, tensile tests were conducted to determine the mechanical properties of the Al 6061-T6. These mechanical properties were then incorporated in the finite element (FE) models generated using LS-DYNA. To validate the FE models, tetra-chiral and reentrant crash plates were produced, and the FE analysis results were compared with the test results. Subsequent to this validation, for each crash box design type (i.e., tetra-chiral cylindrical, tetra-chiral square, reentrant cylindrical, and reentrant square), Kriging surrogate models were constructed using MATLAB for two crash metrics: specific energy absorption (SEA) and crash load efficiency (CLE). Finally, a multi-objective optimization problem was formulated for each crash box design type, the generated Kriging models are integrated into genetic algorithm available in MATLAB, and the Pareto optimal crash box designs were obtained. It was found that the SEA and CLE of reentrant crash boxes were better than those of the tetra-chiral crash boxes. In addition, the reentrant cylindrical crash box displayed better performance than the reentrant square, as well as the tetra-chiral cylindrical and square crash boxes.

ARTICLE HISTORY
Received 9 December 2021
Accepted 2 May 2022

KEYWORDS
Crash box; finite element analysis; Kriging; multi-objective optimization; negative Poisson's ratio

1. Introduction

According to a report by the World Health Organization (WHO) on the prevention of road traffic accidents, more than 3700 people die worldwide every day, on average, due to injuries related to traffic accidents (World Health Organization 2018). While deaths from traffic accidents ranked 9th in the world in 1990, this rose to 3rd place in 2020. It is predicted that these numbers will rise further if necessary preventive measures are not taken. Various safety measures are used in cars to ensure the safety of both the driver and passengers in the event of an accident. These may be considered to be of two types, active and passive safety systems. Active safety systems include equipment (e.g., ABS, EPS, and ASR), which reduce the possibility of accidents by assisting the driver in driving safely. Equipment, such as seat belts, airbags, and crash boxes are passive safety systems that aim to ensure that the occupants of the vehicle are affected at a minimum level in the event of an accident.

Crash boxes absorb the deformation energy coming from the front or rear in the event of an accident and transmit it to the interior of the vehicle at a significantly reduced level. The crash metrics used in crash box designs should be examined in detail to determine the crash efficiency. Various

CONTACT Erdem Acar acar@etu.edu.tr, erdem.acar@gmail.com Department of Mechanical Engineering, TOBB University of Economics and Technology, Söğütözü, Ankara, Turkey.
Communicated by Seonho Cho.

studies have focused on the geometric properties of crash boxes to increase the energy absorption (EA) capacity of crash boxes (Samer, Samaka, and Khalid 2013; Nia and Hamedani 2010). In addition, efforts have been made to develop different types of materials with increased EA capability; this includes filling metallic foam materials into structures (Han, Min, and Cho 2014; Altin, Acar, and Güler 2018) and using composite structures (Saenz-Dominguez et al. 2019). Hexagonal crash boxes were examined by Samer, Samaka, and Khalid (2013) to investigate the effects of magnesium material and trigger structure on crash performance. It was found that as the trigger structure reduced the initial peak load, the EA capacity, and impact force efficiency increased. Nia and Hamedani (2010) investigated the deformation and EA capabilities of thin-walled tubes with various cross-sectional shapes (square, rectangular, circular, hexagonal, triangular, pyramidal, and conical). It was observed that the circular tube has the highest EA capacity and average peak force, while the differences between the maximum and average peak forces in the pyramidal and conical tubes were minimal. Wang et al. (2016) explored the effects of carbon composite density on the EA properties of cylindrical crash boxes under different fiber orientations, wall thicknesses, and loading conditions. It was observed that the EA was more effective under impact loading conditions when compared to quasi-static loading conditions. In addition, it was deduced that the fiber orientation and wall thickness have important effects on the EA performance.

In recent years, there has been a focus on crash absorbers with negative Poisson's ratio (NPR) as a result of innovations in classical production methods and advances in additive manufacturing technology. Structures with NPR, also known as auxetic structures, have excellent mechanical properties, such as better friction resistance, acoustic behavior, EA, fracture strength, and shear modulus (Ma, Lei, Hua, et al. 2018). A substantial number of studies have been performed to investigate the EA capability of auxetic structures owing to their superior EA capabilities. Gao, Ge, et al. (2019) focused on the geometric parameters of double-arrow auxetic crash boxes to achieve better EA performance. In another study by Gao et al. (2018), a new crash box design and optimization were emphasized, where the double-V unit cell structure was proposed as an alternative to thin-walled circular crash boxes. Compared with the thin-walled circular structure, the NPR structure has a lower peak impact force and high energy damping capacity. Liu and Zhang (2009) investigated the in-plane dynamic fracture of triangular and square honeycomb structures. It was found that triangular honeycombs have greater plateau stress than square honeycombs owing to their structural strength; therefore, it has been observed that triangular honeycombs exhibit better EA performance under the same degree of deformation. Lu, Wang, and Chen (2021) compared the EA capacities of star-shaped and stellar circular honeycombs with auxetic cellular structures. They observed that the star cylindrical honeycomb structure has better EA than the star-shaped honeycomb structure, in addition to maintaining its NPR characteristic. Zhou et al. (2016) filled the structure with an NPR structure as a different approach to improve the crash performance of a classical crash box. In that study, a multi-objective optimization study was conducted, and the crash performances of a crash box filled with an NPR structure, a classical crash box, and a crash box filled with aluminum foam were compared. The results showed that the NPR-filled structure positively affected the EA performance and could be a good model for the optimization of NPR structures. Overall, all the aforementioned results show that the crash boxes have better performance owing to the NPR effect.

Reentrant and tetra-chiral unit cell structures are widely used NPR structures in crash boxes because of their excellent EA capability, as discussed in various papers (Yang et al. 2015; Qi et al. 2019; Ma, Lei, Hua, et al. 2018; Ma, Lei, Liang, et al. 2018; Guo et al. 2020). For instance, Ma et al. (2018) investigated the deformation mechanism of chiral structures with four different geometrical properties and showed that they have superior EA and impact prevention properties owing to the twist motion they undergo. Guo et al. (2020) investigated the collision performance of vertically and horizontally oriented structures on reentrant cylindrical crash boxes. It was observed that the EA efficiency of both types of structures increased at high speeds and showed an NPR effect. All these studies show that tetra-chiral and reentrant structures are very useful

alternatives to convectional crash boxes owing to their EA capabilities. In the literature, cylindrical tetra chiral and reentrant crash boxes have been examined individually; however, there is no comparative study on the crashworthiness behavior of square tetra chiral and reentrant crash boxes. In this study, the crash performances of cylindrical as well as square tetra-chiral and reentrant crash boxes are examined simultaneously and crashworthiness behaviors are compared. That is, a comparison of the crash performances of tetra-chiral and reentrant structures is missing in the literature, and this study aims to fill this gap.

High fidelity crashworthiness simulations are computationally costly, therefore, surrogate models (or metamodels) that can imitate the complex behavior of the simulation models accurately while being computationally very efficient have been widely used in the literature. Crashworthiness optimization of the vehicle itself or its components using surrogate models has been conducted by several researchers (Acar 2010; Yildiz and Solanki 2012; Hou et al. 2014; Acar 2015; Niutta et al. 2018; Raponi et al. 2019; Gao, Bai, et al. 2019; Fragoso-Medina and Velázquez-Villegas 2021). In this study, Kriging surrogate models are used owing to their good performance in crash response predictions.

The remainder of this article is organized as follows. Studies on tetra-chiral and reentrant structures are discussed in the next section. In Section 3, the geometric parameters of the tetra-chiral and reentrant structures are explained, and the problem definition is stated. In addition, the requirements for finite element analysis (FEA) are explained, and the crash performance metrics are presented in Section 3. The material characterization tests and crash tests conducted in this study are discussed in Section 4. The details of the FEA modeling of tetra-chiral and reentrant crash boxes, and validation of the FE models are presented in Section 5. The generation of surrogate models is discussed in Section 6, and the optimization results are presented in Section 7. Finally, the article culminates in Section 8, where concluding remarks are provided.

2. Tetra-chiral and reentrant structures

Auxetic cell structures are examined in four basic categories according to the geometrical relations of the unit cell and their deformation mechanisms: reentrant (Yang et al. 2015), with phase converter (Guo et al. 2020), with fixed joint rotation (Qi et al. 2019), and hierarchical structures (Lakes 1993; Wu, Gao, et al. 2018). In this study, tetra-chiral cylinder (Fig. 1a), tetra-chiral square (Fig. 1b), reentrant square (Fig. 1c), and reentrant cylindrical (Fig. 1d) crash boxes were considered.

Prall and Lakes (1997) showed that chiral structures undergo in-plane deformation owing to the effect of NPR. Gao and Zhang (2018) numerically and theoretically investigated the in-plane dynamic response and EA performance of chiral structures. It was observed that the structure absorbed the plastic strain energy in two stages: first, the ligaments were twisted, and then the rigid nodes were bent. In this way, a part of the structure is exposed to plastic deformation after the collision, while the other part remains intact. Wu, Geng, et al. (2018) showed that tetra-chiral cylindrical tubes have a perfect "twist response" mechanism that can convert the incoming axial compression load into a bending deformation. Owing to these characteristics of tetra-chiral cylindrical structures, they may be considered as good alternatives to conventional crash box designs. As a result of the ligaments around the rigid node of the unit cell, a stable load distribution is observed that the forces were smoothly transmitted to the structure to the unit cells in other layers. To improve the mechanical properties of tetra-chiral structures, Li et al. (2019) experimentally investigated the effect of gradients on the energy dissipation performance of structures under crash loading. In gradient tetra-chiral structures, the initial energy dissipation performance can be well controlled, and thus the entire energy dissipation process is smooth. Qi et al. (2017) investigated the in-plane crash responses of tetra-chiral honeycombs under quasi-static and dynamic collision conditions using numerical and experimental methods. Under both quasi-static and dynamic in-plane crushing, the structures showed the NPR effect, but the NPR effect was more pronounced at smaller radius ratios and lower crash speeds. Sgobba (2018) presented the concept

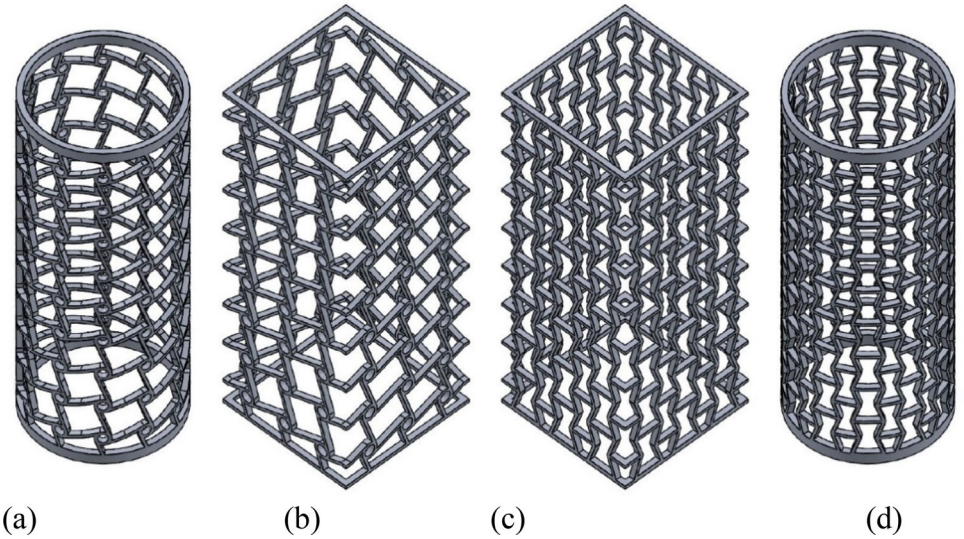

Figure 1. Different types of NPR structures: (a) tetra-chiral cylindrical, (b) tetra-chiral square, (c) Reentrant square, and (d) reentrant cylindrical crash boxes.

of a crash absorber made of a chiral cell filled with polyurethane. Sgobba's experimental and numerical studies demonstrated that the auxetic structure had increased EA capacity. The chiral structure transfers energy to its meshes due to the NPR effect and prevents the foam from expanding during impact. The studies on the tetra-chiral structures showed their improved EA characteristic owing to the NPR effect, and demonstrated that geometric parameters affect the energy dissipation performance significantly.

Reentrant structures are among the most studied auxetic structures. Lee et al. (2019) conducted a comparative study of reentrant structures with conventional and honeycomb structures in terms of axial impact force, specific energy absorption (SEA), and deceleration. Reentrant structures exhibit a lower axial impact force response and higher SEA but lower deceleration than conventional structures. The impact force response and SEA were similar to those of the honeycomb tubes. On the other hand, the honeycomb exhibited oscillatory behavior during deceleration, while the reentrant tube showed a steady downward trend after the first peak force. Hou, Deng, and Zhang (2016) studied the in-plane dynamic collision behavior of a reentrant plate and compared it with a traditional honeycomb structure. According to the results of numerical and analytical studies, the reentrant structure has a higher plateau stress, which indicates that the reentrant structure has better EA ability. As can be clearly seen from these studies, reentrant structures have high EA capabilities owing to NPR effects. Owing to technological developments, the fabrication of structures with auxetic cellular mechanisms has been simplified, increasing the interest of researchers in these structures. The results for these studies show that cylindrical crash boxes have better SEA and crash load efficiency (CLE) values.

3. Problem definition

3.1. Geometric parameters

The geometric parameters that determine the unit cells and boundary dimensions of the tetra-chiral and reentrant crash boxes were assumed to be the same for the four auxetic cell structures considered in this study. The geometric parameters of the tetra-chiral cylindrical and square crash boxes are shown in Fig. 2, and those of the reentrant cylindrical and square crash boxes are shown in Fig. 3. The notations used for the geometric parameters are the same for tetra-chiral and reentrant square and cylindrical crash boxes, and they are based on the study of Ma, Lei, Hua, et al. (2018). The

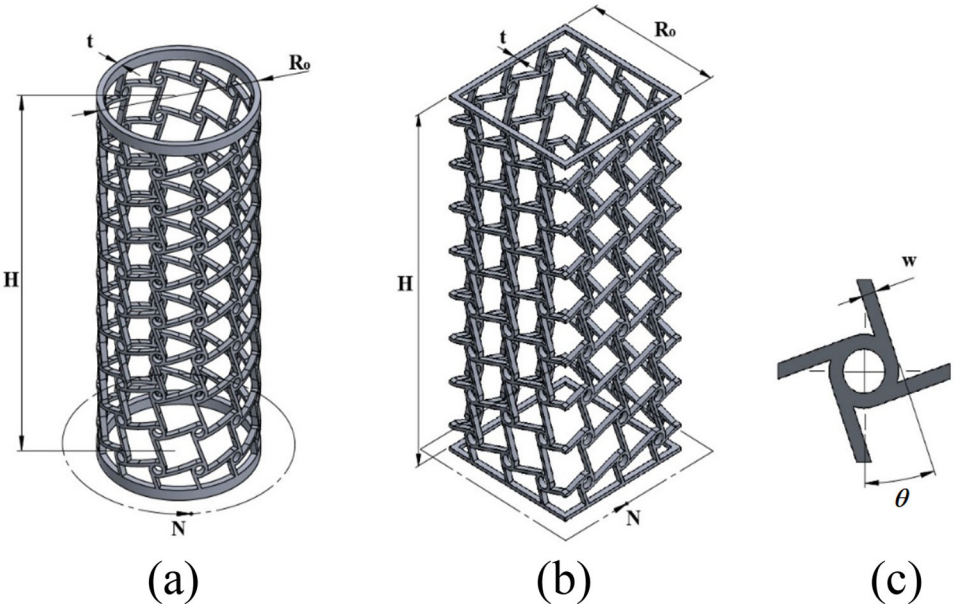

Figure 2. Geometrical properties of the tetra-chiral crash boxes: (a) tetra-chiral cylindrical crash box, (b) tetra-chiral square crash box, and (c) tetra-chiral unit cell.

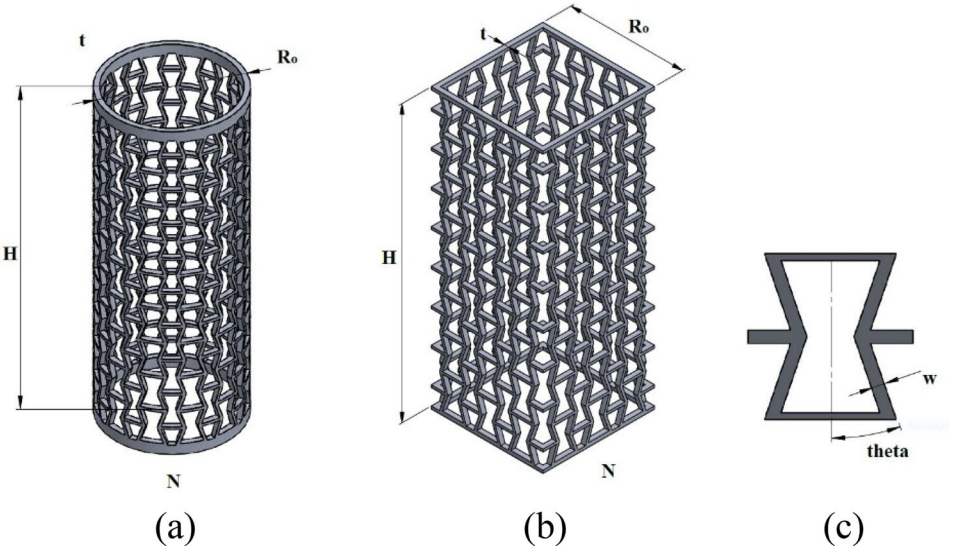

Figure 3. Geometrical properties of the reentrant crash boxes: (a) reentrant cylindrical crash box, (b) reentrant square crash box, and (c) reentrant unit cell.

geometric parameters used in the design of crash boxes are as follows: the height of the crash box (H), the outer radius of the cylindrical crash box or the cross-sectional side length of the square crash box, (R_o), the circumferential number of unit cells (N), the thickness of the crash box (t), the width of the ligament (w), and the angle of ligaments between axial directions $(\theta$, in degrees).

All the crash boxes have a height of $H = 200$ mm and an outer length (diameter for circular and side length for square) of $R_o = 80$ mm. The height of the crash boxes was determined in such a way that it allowed a minimum crush displacement of $d = 60$ mm at the time of collision.

The outer diameter values were selected in accordance with ASTM-B241, which is a standard for manufacturing dimensions of seamless aluminum and aluminum alloy tubing.

Based on the limitations of our manufacturing facilities and the experience of the authors, the ranges of N, t, w, and θ values required to determine the optimum crash box design parameters are selected as follows: $14 \leq \theta \leq 22$, $1.5 \leq w \leq 2.5$, $2 \leq t \leq 6$, and $8 \leq N \leq 16$. The nominal values of these parameters are taken from Ma, Lei, Hua, et al. (2018), and the ranges of these parameters are determined to obtain various tetra-chiral and reentrant square and cylindrical crash boxes with diverse sizes and crashworthiness behavior.

3.2. Crash metrics

Different crash metrics are available in the literature to evaluate the performance of crash boxes (Altin, Acar, and Güler 2021; Abbasi et al. 2015). The metrics used in this study are explained in the following subsections.

3.2.1. Total energy absorption (EA)

The total energy absorption (EA) is defined as the work performed by the energy released during the collision process. The area under the force-displacement graph (Fig. 4) gives the total energy absorbed, and it is calculated using Eq. (1), where F is the crash force and d is the final deformation distance of the wall. In this study, d was set to 60 mm.

$$\mathrm{EA} = \int_0^d F(x)dx \tag{1}$$

3.2.2. Specific energy absorption (SEA)

The vehicles are designed to keep the mass of the body-in-white to a minimum while satisfying the safety requirements. In this context, mass is an important parameter when designing a crash box. SEA is an important criterion used to measure the EA capacity per unit mass of the structure, which is obtained by dividing the total absorbed energy, as shown in Eq. (2) by the pre-collision mass (m) of the structure.

$$\mathrm{SEA} = \frac{\mathrm{EA}}{m} \tag{2}$$

3.2.3. Mean crushing force (MCF)

The mean crushing force (MCF) is the average force obtained by dividing the total energy absorbed at the time of collision by the total displacement, as given in Eq. (3).

$$\mathrm{MCF} = \frac{\mathrm{EA}}{d} \tag{3}$$

3.2.4. Peak crushing force (PCF)

For an ideal crash box, the peak crushing force (PCF) acting inside the vehicle should be minimal to ensure passenger safety. The PCF to a crash box is expected to be as low as possible and close to the average crush force.

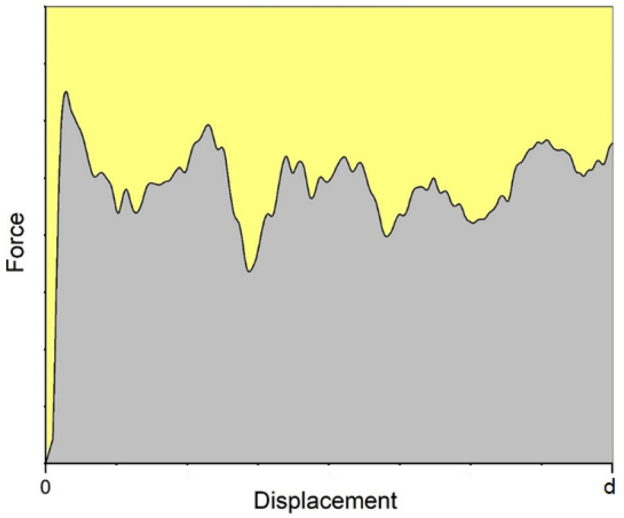

Figure 4. A typical force–displacement curve for a vehicle structure.

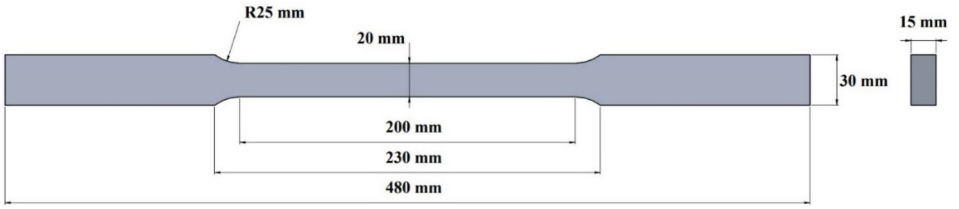

Figure 5. Dimensions of the tensile specimens used.

3.2.5. Crash load efficiency

CLE is another important criterion obtained by dividing the average impact force by the peak crash force and is calculated as shown in Eq. (4). Larger CLE values indicate a better performance of an energy absorber.

$$\mathrm{CLE} = \frac{\mathrm{MCF}}{\mathrm{PCF}} \tag{4}$$

In this study, force–displacement figures were obtained with LS-PREPOST as the outputs of the FE analysis, and EA and PCF were evaluated using ORIGIN PRO software. Finally, SEA and CLE values were calculated using the EA, PCF, and mass values.

4. Experimental studies

4.1. Material characterization tests

The 6061-T6 aluminum material has attracted attention owing to its high yield strength (Bernard 1977) and ductile behavior (Isabell and Christman 1970). In the experimental study of Christman et al. (1977) regarding the dynamic properties of 6061-T6 aluminum, the material exhibited excellent elasto-plastic behavior under uniaxial compression loading. Owing to these superior features, 6061-T6 aluminum material was used in the design of crash boxes in this study.

Tensile tests were performed to determine the mechanical properties of the 6061-T6 aluminum material (for use in FEA analyses). Three test specimens, with the dimensions specified in Fig. 5,

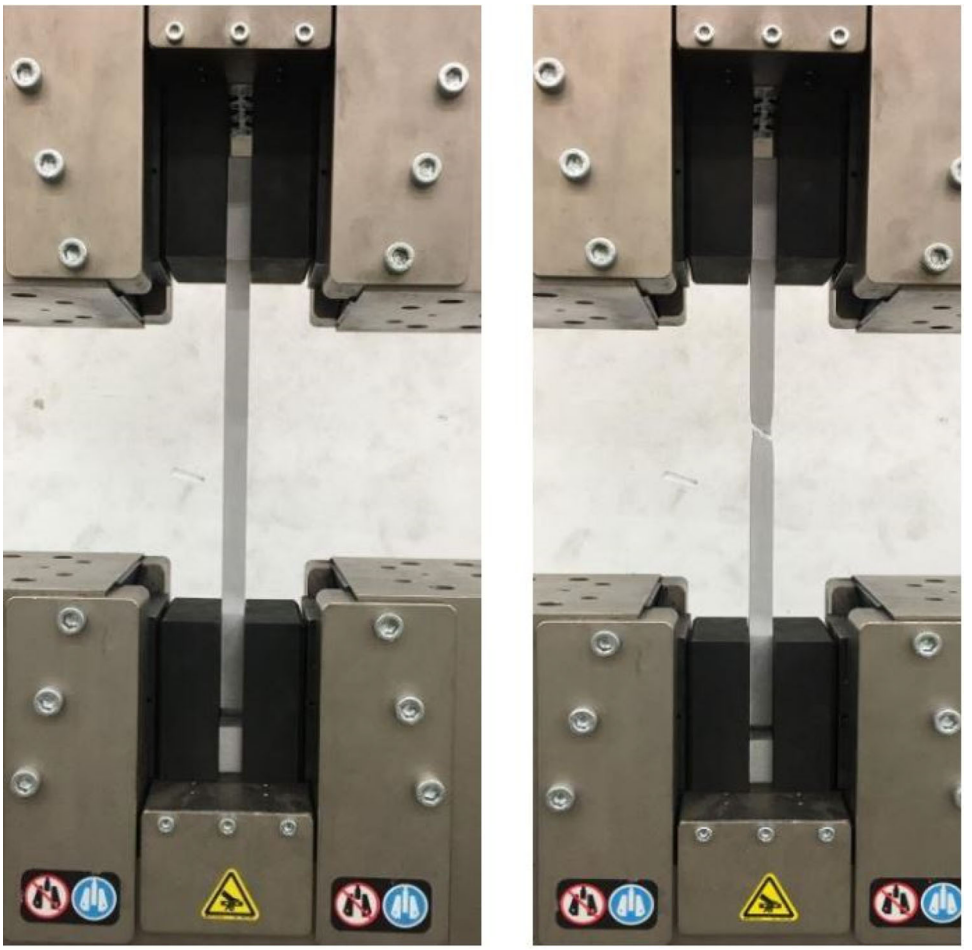

Figure 6. Specimen in the crosshead of the tensile test machine (a) before test and (b) after fracture.

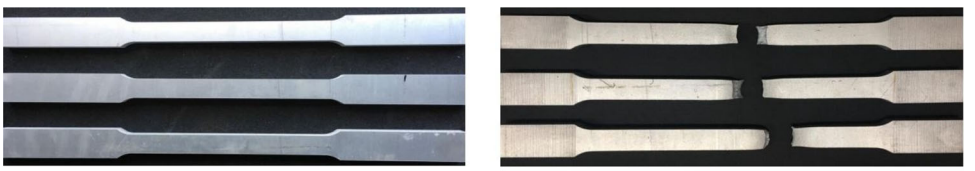

Figure 7. Test specimens (a) before test and (b) after test.

were prepared according to the ASTM-E8 standard for tensile tests. The specimens were processed in a CNC water jet machine to prevent the deterioration of their chemical and mechanical properties. The tests were performed in accordance with the ASTM-E8 test procedure on a universal testing machine, located at the Technology Center of the TOBB University of Economics

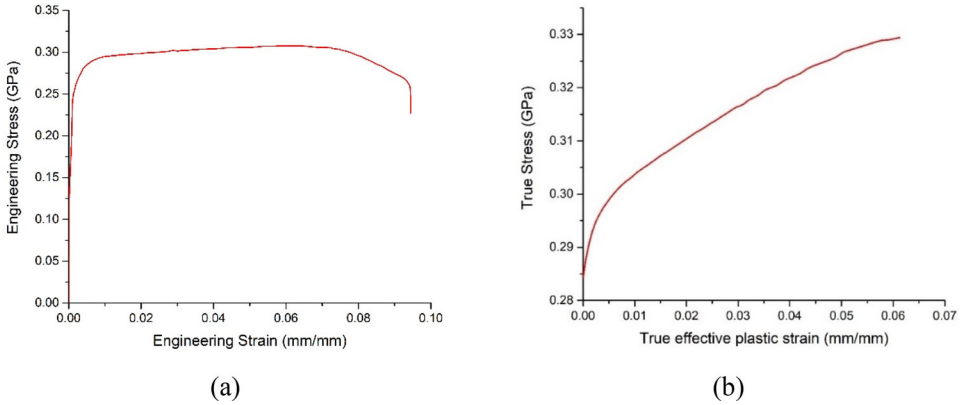

Figure 8. (a) Engineering stress-strain curve and (b) true stress – true strain curve of 6061-T6 alloy.

Table 1. Mechanical Properties of 6061-T6 alloy.

Density [kg/m^3]	Poisson's ratio	Modulus of elasticity [GPa]	Yield strength [MPa]
2700	0.33	68.85	285

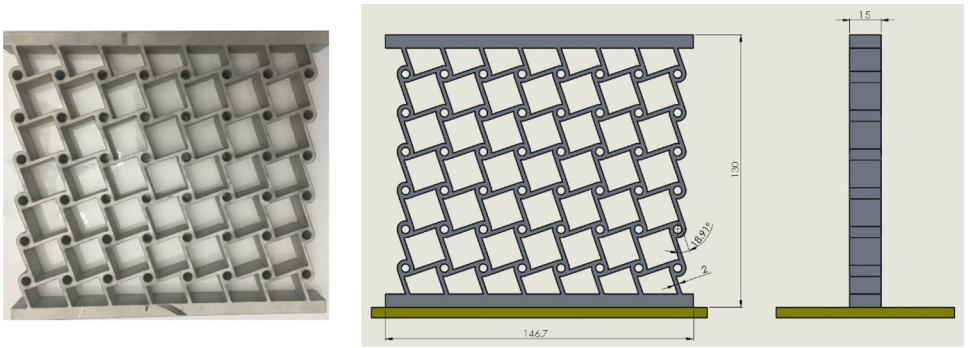

(a) Tetra-chiral crushing plate.

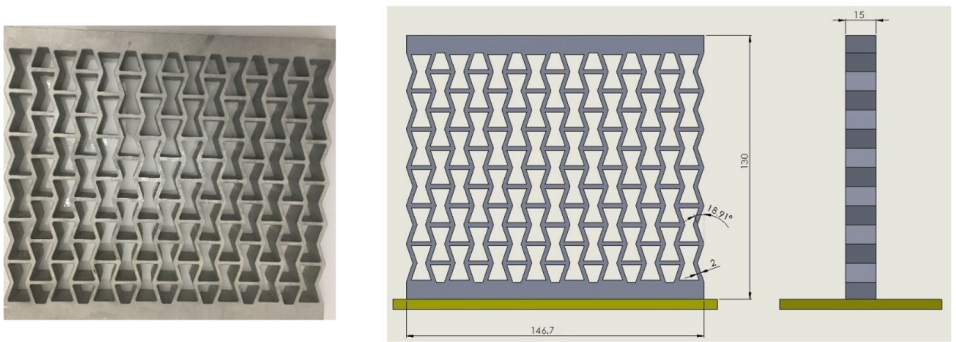

(b) Re-entrant crushing plate

Figure 9. Geometrical properties of the tetra-chiral and the reentrant crushing plates.

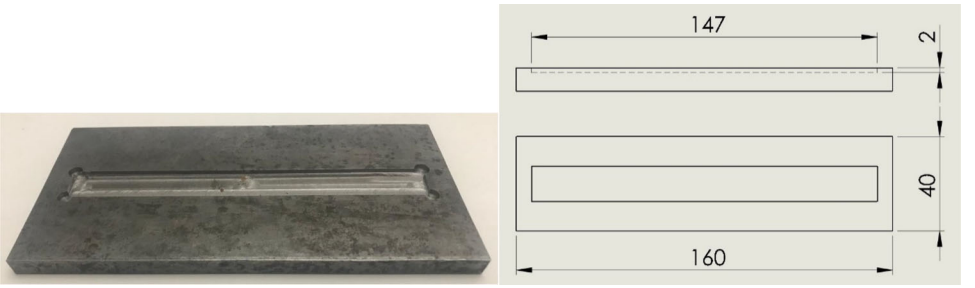

Figure 10. Dimensions of the base plate.

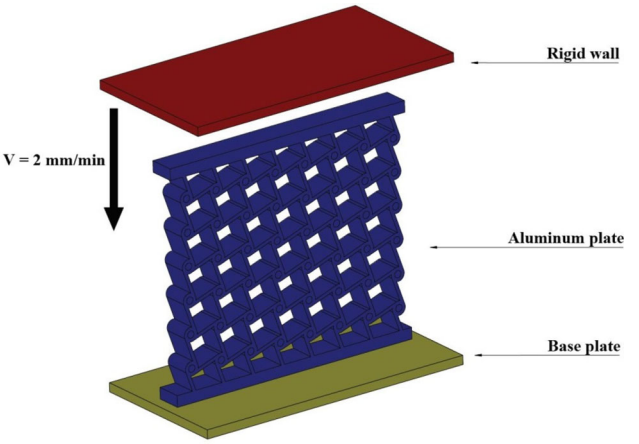

Figure 11. Auxetic plate crushing test conditions.

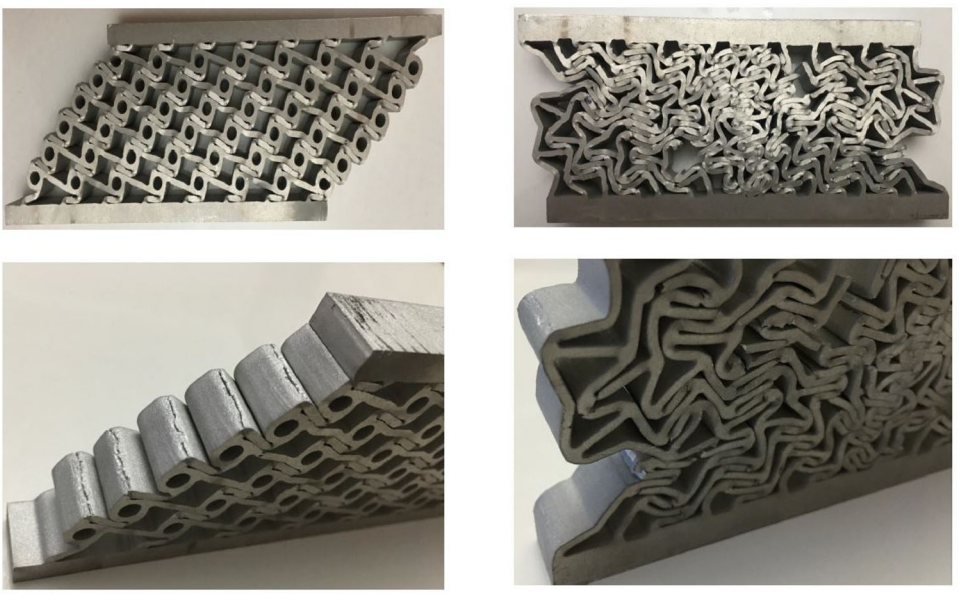

Figure 12. Deformed views of (a) tetra-chiral plate and (b) reentrant plate.

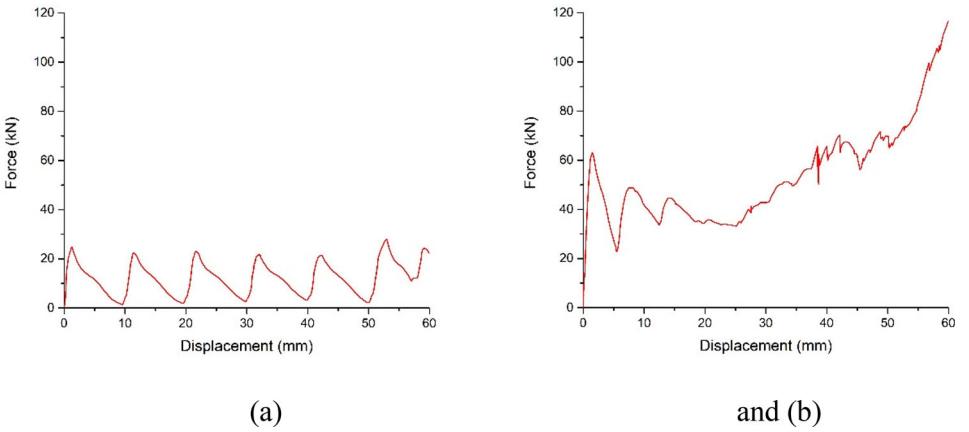

Figure 13. Force-displacement curves of (a) tetra-chiral plate and (b) reentrant plate.

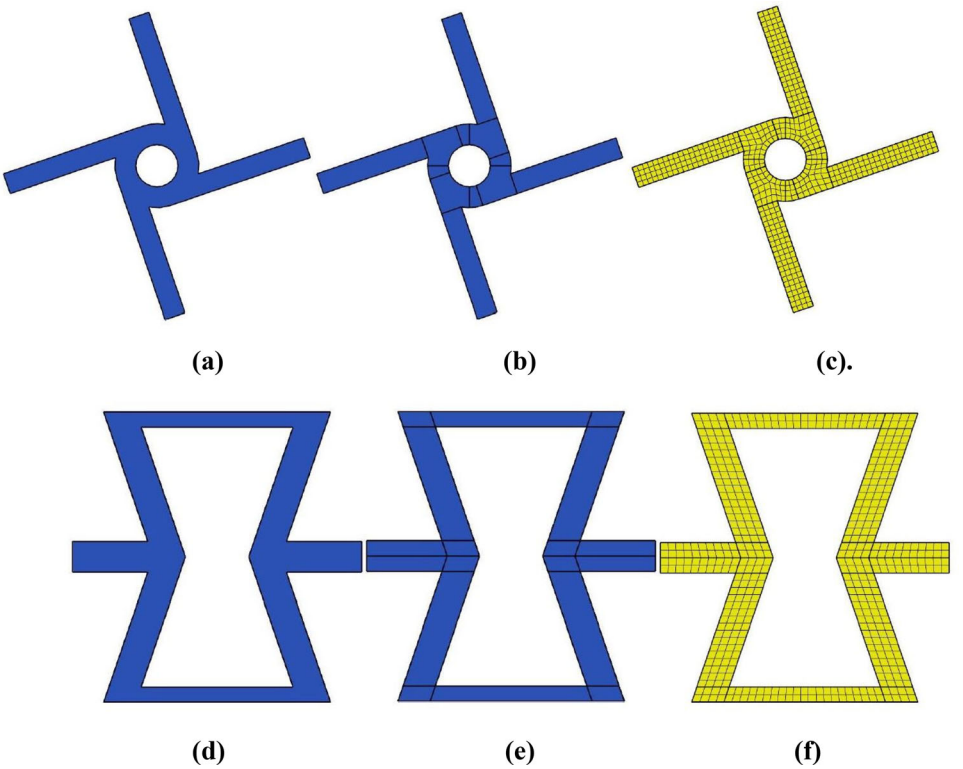

Figure 14. Tetra-chiral unit cell mesh preparation steps: (a) CAD modeling, (b) separation into blocks, (c) meshing; and reentrant unit cell mesh preparation steps: (d) CAD modeling, (e) separation into blocks, and (f) meshing.

and Technology, with a capacity of 600 kN (Fig. 6). The tensile test specimens before and after the test are shown in Fig. 7.

The mechanical properties of the material, calculated according to the engineering stress–strain curve (Fig. 8) obtained from the tensile test, are listed in Table 1. The true stress-true effective plastic strain curve obtained with the formulation specified on the LS-DYNA support page (LS-DYNA Support 2021) is shown in Fig. 8 These mechanical properties and stress–strain curves were used to prepare the LS-DYNA material card.

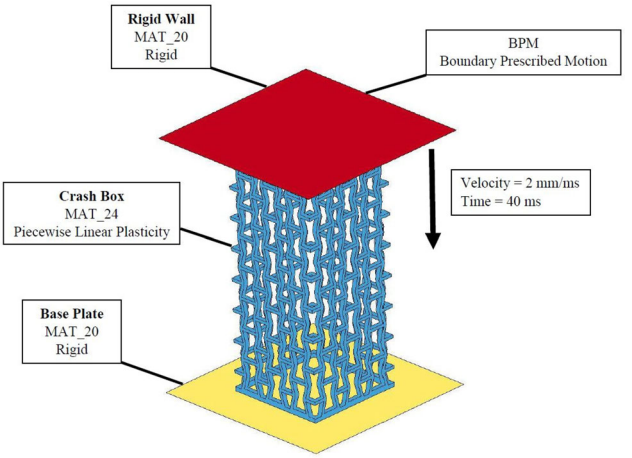

Figure 15. Finite element model.

4.2. Crash tests

To validate the accuracy of the quasi-static FEA of the crash boxes, tetra-chiral (Fig. 9a) and reentrant (Fig. 9b) plates with the same geometrical properties were machined on a CNC waterjet machine from a 6061-T6 aluminum plate with a thickness of 15 mm, on which the tensile samples were prepared. To fix the auxetic structures during the crush test, the base plates were machined on a CNC milling machine from SAE 1040 steel material. Figure 10 shows that a 2 mm deep cavity is machined on the steel plate to accommodate the lower surfaces of the tetra-chiral and reentrant structures.

With the test conditions shown schematically in Fig. 11, crash tests were also carried out at a compression speed of 2 mm/min on a universal testing machine with a capacity of 600 kN, located at the Technology Center of the TOBB University of Economics and Technology. After the crushing test performed on the tetra-chiral plate, uniform stacking of the unit cells on the beams and a symmetrical break at the linkup of the ligaments to the rigid nodes was observed (Fig. 12a). It should be noted that Fig. 12a shows the tetra chiral plate used for validation of FEA only. This plate is not used as the part of the vehicle structure. In this paper, cylindrical or square tubular auxetic structures are proposed to be used as crash boxes. While the tetra chiral plate in Fig. 12a shows larger envelope under deformation, the deformation behavior of the cylindrical or square tubular auxetic structures are different. For the tubular auxetic structures, twisting response is observed under deformation.

Inward shrinkage is observed on the reentrant plate owing to the NPR effect, and an unsymmetrical fracture is seen in Fig. 12b. The force-displacement data are shown in Fig. 13 and were obtained for validating the FE models.

5. Numerical studies

5.1. Finite element modeling

For the preliminary preparation of the FEA, solid models were prepared using SolidWorks software, and then FE meshes were created using HYPERMESH software. Owing to the complex nature of the geometries, mesh geometries were prepared for both tetra-chiral and reentrant structures before mesh creation (Fig. 14). This approach is also applied for mesh preparation studies within the optimum design framework for tetra-chiral and reentrant square and cylindrical crash boxes. Solid hexahedron mesh elements were used for all crash boxes, and shell quadrilateral mesh elements were

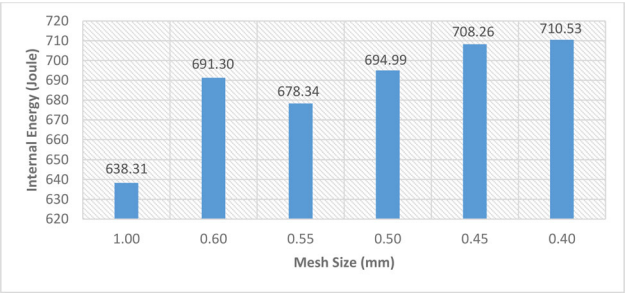

Figure 16. Mesh sensitivity analysis for tetra-chiral crash box.

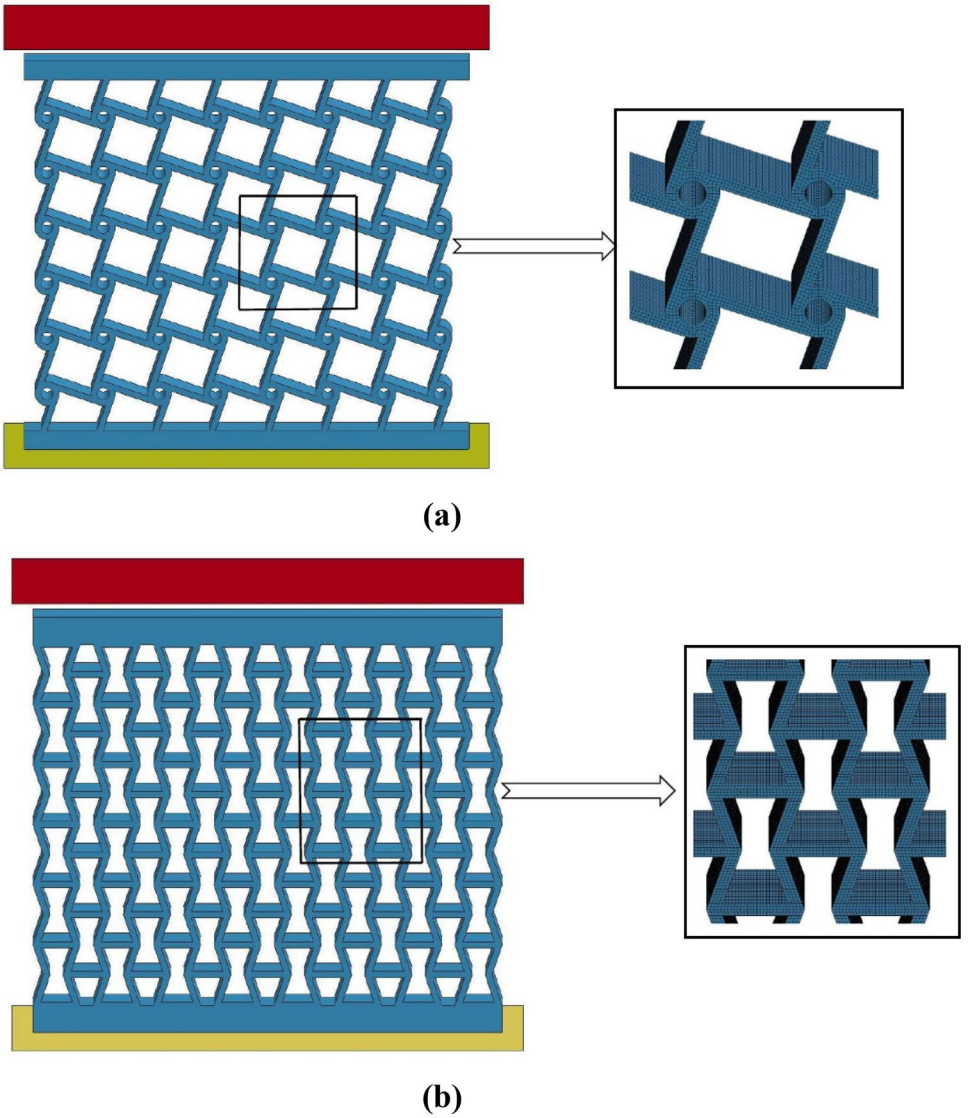

Figure 17. (a) Tetra-chiral and (b) reentrant validation model.

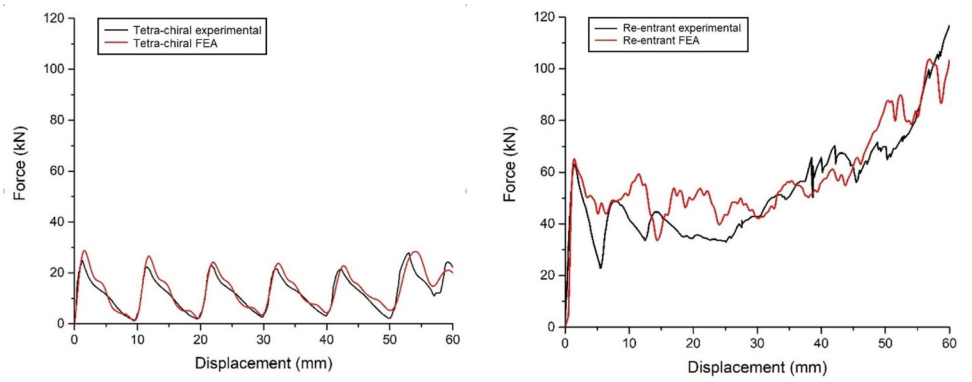

(a) (b)

Figure 18. Force-displacement curves for experimental and FEA of (a) tetra-chiral plate and (b) reentrant plate.

used for the moving plates. In addition, the mesh qualities for all models were checked according to the aspect ratio, Jacobian ratio, warping ratio, and skewness values. For the aspect ratio, the ideal value was 1, while values less than five were considered acceptable. For the Jacobian ratio, the ideal value is 1; however, values greater than 0.5, were considered acceptable. For the warp angle, the ideal value was 0°, with values less than 30° considered acceptable. Finally, for skewness, the ideal value was 0°, with values less than 45° being considered acceptable.

The FEA model was prepared using LS-PREPOST, and it was solved using a general-purpose FEA software LS-DYNA to determine the crash performance of the crash boxes. The material card "Piecewise linear plasticity (MAT_24)" was used to model the crash box material, and it was modeled with constant stress solid elements. In addition, the mechanical properties and stress-strain curve data used in the MAT_24 card values were obtained from the 6061-T6 tensile test (see Fig. 9). Moreover, the non-deforming material card "Rigid (MAT_20)" is chosen for the movable rigid wall and base plate. Additionally, a Belytschko – Tsay card was chosen as the hourglass control type to prevent hourglass events. "Boundary projected motion (BPM) is applied to the moving rigid wall in the direction of the crash box top surface at a velocity of 2 mm/ms for a duration of 30 ms. Note that this velocity value is different from the velocity value used in the tests, that is, 2 mm/min. FE analyses are considered quasi-static because the dynamic effects are excluded, and the velocity value used in this study is much smaller than the ballistic velocities. It is observed that the kinetic energy is negligible compared to the deformation energy because the crash velocities are low (kinetic energy is 0.09% of the total energy). Therefore, the low kinetic energy of the system indicates that the inertial forces are negligible. The AUTOMATIC_SURFACE_TO_ SURFACE" algorithm was used to model contact between the rigid wall and crash box to avoid interference between the contacting parts. Furthermore, the static and dynamic friction coefficients are taken as 0.3 and 0.2, respectively, as in our earlier work (Altin, Acar, and Güler 2018). The AUTOMATIC_SINGLE_ SURFACE" contact algorithm was used to prevent each structure from interfering with itself. The FE model with boundary conditions and LS-DYNA cards is presented in Fig. 15.

5.2. Mesh sensitivity analysis

To determine the appropriate finite element mesh size, a convergence analysis was performed. The variation of the internal energy with respect to the mesh size was monitored to determine the appropriate mesh size. Figure 16 shows that the convergence of the internal energy with respect to the mesh size is achieved when the element size is 0.45 mm, for the tetra-chiral crash box.

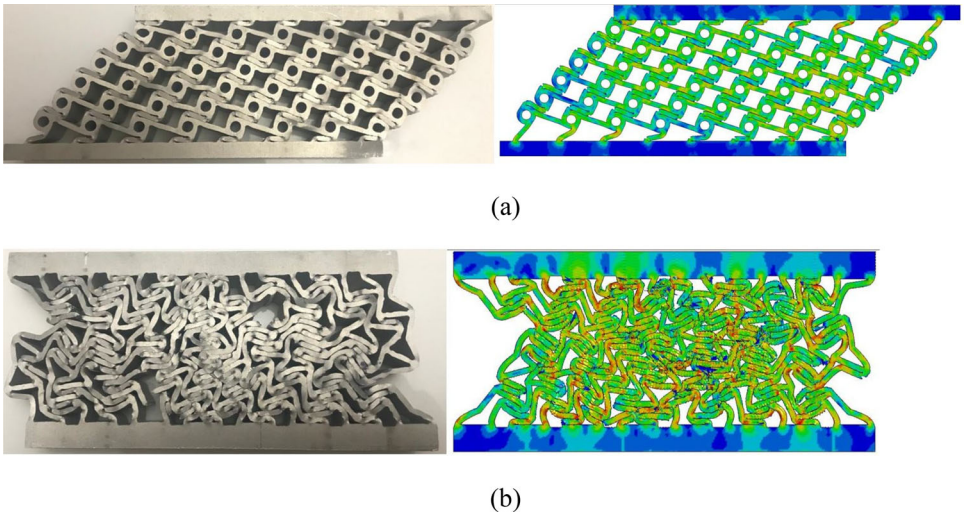

Figure 19. (a) Tetra-chiral and (b) reentrant plates deformation zones.

Table 2. Tetra-chiral plate crash performance metrics.

	EA [kJ]	SEA [kJ/kg]	PCF [kN]	MCF [kN]	CLE
Experimental	0.731	3.132	27.92	12.19	0.437
FEA study	0.806	3.465	28.76	13.43	0.467
Error (%)	9.3	9.6	2.9	9.2	6.4

Table 3. Reentrant plate crash performance metrics.

	EA [kJ]	SEA [kJ/kg]	PCF [kN]	MCF [kN]	CLE
Experimental	3.231	10.15	111.8	53.85	0.482
FEA study	3.495	10.98	108.8	58.25	0.535
Error (%)	7.5	7.5	2.6	7.5	9.9

5.3. Validation of finite element analysis

The crash tests discussed in Section 4 were used to validate the finite element model. The geometric properties of the validation plates are as follows: the length is 130 mm on the vertical axis, 146.7 mm on the horizontal axis, $w = 2$ mm, $t = 15$ mm, $\theta = 18.31°$, the number of unit cells on the horizontal axis is 8, and finally the number of unit cells on the vertical axis is 6. The mesh models are prepared for the FEA, for which the element size is set as 0.45 mm as determined in the sensitivity analysis. While preparing the FE models, all steps described in the previous sections were performed. The tetra-chiral and reentrant models are shown in Fig. 17a and 17b, respectively.

The force displacement curves obtained from the FEA and experiments for the tetra-chiral and reentrant plates are shown in Fig. 18a and 18b, respectively. It can be seen that the peak forces obtained in FEA for each fold match the corresponding experimental values, and the overall trends are very similar. In the tetra-chiral plate, progressive local buckling and symmetric deformation are observed until 55 mm deformation, which gives periodic force-displacement behavior as shown in Fig. 18a. The fold formation in tetra-chiral plate can be seen easily. Notice that after 55 mm deformation, the densification starts. However, in the reentrant plate, periodic force-displacement behavior is not seen due to inward shrinkage and unsymmetrical deformation. Up to 20 mm deformation, the folding behavior can be observed, then the structure is stacked and the densification starts.

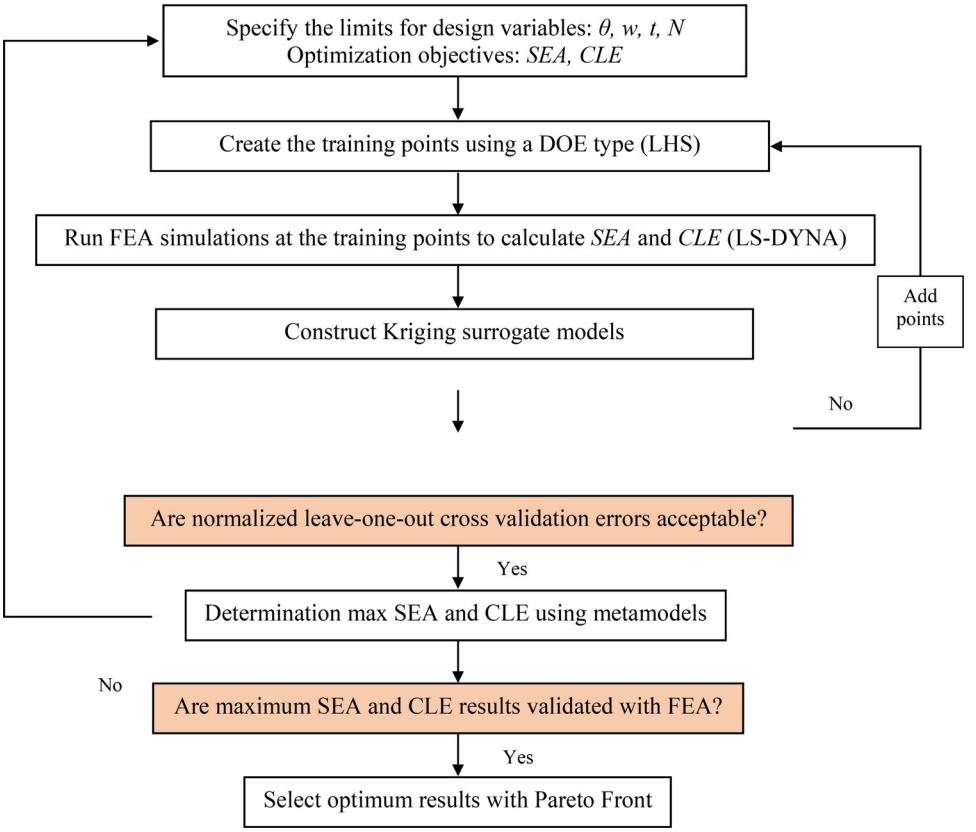

Figure 20. Flowchart of the surrogate-based multi-objective optimization process.

When the deformation shapes observed in the crush tests and FEA studies were compared, it was observed that the deformation zones and types were similar (see Fig. 19a and 19b). The crash metrics and percentage errors in Tables 2 and 3 show that the errors are within an acceptable range (all values are smaller than 10%).

6. Multi-objective optimization using surrogate models

6.1. Description of the optimization problem

The design variables for this study were the angle of ligaments between axial directions (θ), the width of ligament (w), the thickness of the crash box (t), and the circumferential number of the unit cells (N). The lower and upper bounds of these variables are discussed in Section 2. The performances of the crash boxes were evaluated using SEA and CLE. Thus, the optimization problem can be expressed as

$$\begin{aligned} &\text{Find} && \theta,\ w,\ t,\ N \\ &\text{Max} && \{\text{SEA},\ \text{CLE}\} \\ &\text{S.t.} && 14^{\circ} \leq \theta \leq 22^{\circ} \\ & && 1.5\ \text{mm} \leq w \leq 2.5\ \text{mm} \\ & && 2\ \text{mm} \leq t \leq 6\ \text{mm} \\ & && 8 \leq N \leq 16 \end{aligned} \tag{5}$$

Table 4. Normalized root mean square leave-one-out cross validation errors.

Crash box type	Crash metric	$nRMSE_{XV}$ (%)
Tetra-chiral cylindrical (TC)	SEA [kJ/kg]	5.7
	CLE	8.7
Tetra-chiral square (TS)	SEA [kJ/kg]	8.3
	CLE	8.0
Reentrant cylindrical (RC)	SEA [kJ/kg]	12.5
	CLE	14.9
Reentrant square (RS)	SEA [kJ/kg]	8.0
	CLE	9.8

In this study, this multi-objective optimization problem is solved by defining a composite (or aggregate) objective function (see Eq. 6) to capture the Pareto-optimal points.

$$f = \alpha \frac{\text{SEA}}{\text{SEA}_{\max}} + (1-\alpha)\frac{\text{CLE}}{\text{CLE}_{\max}} \tag{6}$$

where f is the composite objective function to be maximized, and α is a weight factor used to adjust the relative importance of SEA and CLE, and is varied between 0 and 1 to obtain the corresponding Pareto optimal points. The terms $\text{SEA}_{\max}$ and $\text{CLE}_{\max}$ are respectively, the maximum values of the SEA and CLE responses observed at the training points.

Figure 20 shows the surrogate-based multi-objective optimization flowchart of the crash boxes. First, the design variables, their limits, and optimization objectives were defined, as in the previous sections. Then, the data points were selected by the Latin hypercube sampling (LHS) method, and the corresponding response values (*SEA* and *CLE*) were obtained through the FE analyses. After the responses were computed using FEA, the Kriging model was constructed. If the accuracies of the surrogate models were found to be acceptable, the maximum *SEA* and *CLE* values were determined by integrating the Kriging models into a genetic algorithm. Finally, Pareto optimum solutions were obtained by optimizing the composite function.

In this study, the "gamultiobj" built-in function of MATLAB is used. This function uses a controlled, elitist genetic algorithm (Isabell and Christman 1970), and creates a series of points on Pareto front. An elitist genetic algorithm always favors individuals with better fitness value (rank). A controlled elitist genetic algorithm also favors individuals that can help increase the diversity of the population even if they have a lower fitness value.

6.2. Determination of training data points

The LHS method, a gap filling technique, was used to determine the DOE points in this study. For each crash box design type (i.e., tetra-chiral cylindrical, tetra-chiral square, reentrant cylindrical, and reentrant square), 40 training points (10 times the number of design variables following the recommendation of Jones, Schonlau, and Welch (1998)) were generated. The data points generated for the square and cylindrical crash boxes are given in the Appendix.

Because four different crash box types were considered in this study, 160 crash box analysis models were prepared, and crash analyses were performed using LS-DYNA to calculate the *SEA* and *CLE* values. The calculated *SEA* and *CLE* values are provided in the Appendix.

6.3. Surrogate model errors

Different metrics can be applied to validate the accuracy of surrogate models. In this study, leave-one-out root mean square cross-validation error metrics (RMSE_{XV}) were used since the Kriging model passes through data points. RMSE_{XV} is calculated as follows: Assuming there are n training data points, a surrogate model is generated n times, excluding one data point each time. Next,

Table 5. Single objective optimization results and comparison to validation runs.

Crash box type	Crash metric	Kriging pred.	LS-DYNA result	Error %	Design variables			
					θ (deg)	w (mm)	t (mm)	N
TC	SEA [kJ/kg]	4.430	4.474	1.0	20.41	2.496	4.886	16
	CLE	0.622	0.627	0.8	21.95	2.482	3.296	15
TS	SEA [kJ/kg]	3.857	3.977	3.0	20.11	2.492	5.573	16
	CLE	0.602	0.613	1.8	21.95	2.185	5.760	16
RC	SEA [kJ/kg]	6.830	6.961	1.9	17.24	2.388	5.626	13
	CLE	0.686	0.652	5.0	21.91	2.013	5.958	8
RS	SEA [kJ/kg]	5.467	5.259	3.8	14.12	2.480	5.974	16
	CLE	0.782	0.753	3.7	21.93	1.514	5.948	8

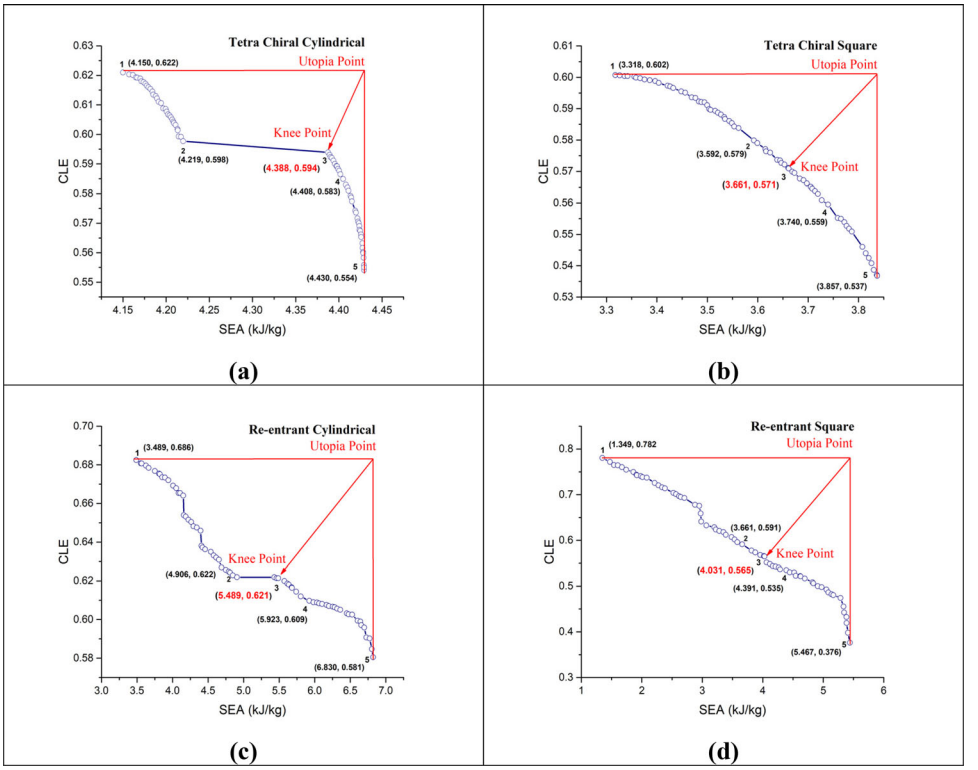

Figure 21. Pareto optimal designs for (a) tetra-chiral cylindrical (TC), (b) tetra-chiral square (TS), (c) reentrant cylindrical (RC), and (d) reentrant square (RS) crash boxes.

the difference between the actual response (y_k) of the skipped data point and the predicted response $(\hat{y}_k^{(-k)})$ is calculated by constructing a surrogate model.

$$\mathrm{RMSE}_{\mathrm{XV}} = \sqrt{\frac{1}{n}\sum_{k=1}^{n}\left(y_k - \hat{y}_k^{(-k)}\right)^2} \tag{7}$$

Finally, the GMSE values are normalized by dividing them by the range of the response values observed at the data points (see Eq. (8)), where $y_{\max}$ and $y_{\max}$ are the maximum and minimum values of the response at the data points, respectively.

$$\mathrm{nRMSE}_{\mathrm{XV}} = \frac{\mathrm{RMSE}_{\mathrm{XV}}}{y_{\max} - y_{\min}} \tag{8}$$

Table 6. Multi-objective optimization results (knee points).

	Design variables				Responses	
Crash box type	θ (deg)	w (mm)	T (mm)	N	SEA (kJ/kg)	CLE
TC	21.9	2.5	3.5	16	4.388	0.594
TS	21.0	2.4	5.7	16	3.661	0.571
RC	18.5	2.0	4.6	13	5.489	0.621
RS	21.6	2.5	5.8	12	4.031	0.565

The normalized root mean square leave-one-out cross-validation error ($nRMSE_{XV}$) values calculated for the Kriging models are shown in Table 4. The $nRMSE_{XV}$ values of the Kriging models created for predicting the *SEA* and *CLE* responses of the tetra-chiral crash boxes were below 10%. Similarly, the $nRMSE_{XV}$ values of the Kriging models created for predicting the SEA responses of the reentrant crash boxes were also below 10%. On the other hand, the $nRMSE_{XV}$ value of the Kriging model created for predicting the *CLE* of the RC box was 13.4%, *and that* of the RS crash box was 10.4%. These error values were found to be acceptable for predicting the response of a nonlinear phenomenon such as a crash.

7. Optimization results

7.1. Single objective optimization results

The constructed Kriging models were incorporated into the MATLAB genetic algorithm optimizer. Before solving the optimization problem given in Eq. (5), single-objective optimization studies were conducted to validate the optimization framework, that is, the crash boxes are optimized for maximum *SEA* and maximum *CLE*, respectively, using Kriging models, and the Kriging model optimum solutions were validated using LS-DYNA. Table 5 shows the optimum geometric parameters (θ, w, t, N), as well as the corresponding *SEA* and *CLE* values. FE models for the optimum TC, TS, RC, and RS crash boxes were prepared, and crash simulations were performed. The errors in the Kriging model predictions were all found to be smaller than 5%.

7.2. Multi-objective optimization results

For multi-objective optimization problems, it is necessary to consider each objective in the solution space, and the solution comprises a set of Pareto optimal designs (Acar et al. 2011; Zhou et al. 2016). Figure 21 shows these Pareto optimal designs with the corresponding *SEA* and *CLE* values. Optimum design points #1 and #5 are associated with the maximum *CLE* and maximum *SEA* values, respectively. The utopia point is an unachievable point with maximum *SEA* and *CLE* values. Optimum design #3 is known as the knee point, and is the closest Pareto optimal design to the utopia point (or the solution on the Pareto front with the maximum marginal utility) (Zhou et al. 2016).

Table 6 shows the optimum values of the design variables and the corresponding *SEA* and *CLE* values of the four crash box types. The RC crash box had the highest *SEA* value (5.489 kJ/kg) among the four types; the corresponding values for TC, RS, and TS were 4.388 kJ/kg (20.1% smaller), 4.031 kJ/kg (26.6% smaller), and 3.661 kJ/kg (33.3% smaller), respectively. Similarly, the *CLE* value for the RC crash box was the largest at 0.621. The corresponding values for the TC, TS, and RS crash boxes were 0.594 (4.3% smaller), 0.571 (8.1%), 0.565 (9.0% smaller), respectively. It is thus concluded that among these four crash box types, the RC crash box type has the maximum *SEA* and *CLE* values.

8. Concluding remarks

In this study, the crashworthiness performance of cylindrical and square crash boxes with tetra-chiral and reentrant cell structures (two widely used NPR structures) were investigated both experimentally and numerically and optimized in terms of CLE and SEA. The following conclusions were drawn from the results:

- For both tetra-chiral and reentrant crash boxes, when cylindrical and square cross sections were compared, cylindrical crash boxes with the same geometric dimensions had higher *SEA* values because they were more stable, and the *CLE* values were quite close to each other.
- When tetra-chiral and reentrant crash boxes were compared, it was observed that the tetra-chiral structure reduced the initial peak forces owing to its twisting response. For reentrant structures, the initial peak forces were higher as the material behaves more rigidly. In addition, reentrant structures have a long plateau stress range, resulting in higher *CLE* and *SEA* values compared to the tetra-chiral structures.
- Among the four crash box types considered (RC, TS, RC, and RS), it was found that the RC crash box had the highest *SEA* value. The values for the TC, RS, and TS crash boxes were smaller by 20.1%, 26.6%, and 33.3%, respectively.
- In terms of *CLE*, RC had the largest *CLE* value. The values for TC, TS, and RS were smaller by 4.3%, 8.1%, and 9.0%, respectively.

The deformation modes and EA characteristics of the four types of crash boxes are discussed above. It should be noted that the investigation of the NPR effect is missing in this study, and considered as a subject of a future study.

Acknowledgments

Material characterization tests and crash tests were conducted at the Technology Center of the TOBB University of Economics and Technology, Ankara, Turkey. The support from the Technology Center is gratefully acknowledged.

Disclosure statement

The authors declare that they have no known competing financial interests or personal relationships that could have influenced the work reported in this article.

CRediT authorship contribution statement

C. Aktaş: conceptualization, methodology, formal analysis, investigation, visualization, and writing – original draft. **E. Acar:** Conceptualization, Methodology, Writing – review and editing, Supervision. **M. A. Güler:** Conceptualization, Methodology, Writing – Review and Editing, Supervision. **M. Altı n:** Conceptualization, Methodology, Writing – Review and Editing.

References

Abbasi, M., S. Reddy, A. Ghafari-Nazari, and M. Fard. 2015. Multiobjective crashworthiness optimization of multi-cornered thin-walled sheet metal members. *Thin-Walled Structures* 89:31–41. doi:10.1016/j.tws.2014.12.009.

Acar, E. 2010. Optimizing the shape parameters of radial basis functions: An application to automobile crashworthiness. *Proceedings of the Institution of Mechanical Engineers, Part D: Journal of Automobile Engineering* 224 (12):1541–53. doi:10.1243/09544070JAUTO1560.

Acar, E. 2015. Increasing automobile crash response metamodel accuracy through adjusted cross validation error based on outlier analysis. *International Journal of Crashworthiness* 20 (2):107–22. doi:10.1080/13588265.2014.977839.

Acar, E., M. A. Guler, B. Gerceker, M. E. Cerit, and B. Bayram. 2011. Multi-objective crashworthiness optimization of tapered thin-walled tubes with axisymmetric indentations. *Thin-Walled Structures* 49 (1):94–105. doi:10.1016/j.tws.2010.08.010.

Altin, M., E. Acar, and M. A. Güler. 2018. Foam filling options for crashworthiness optimization of thin-walled multi-tubular circular columns. *Thin-Walled Structures* 131:309–23. doi:10.1016/j.tws.2018.06.043.

Altin, M., E. Acar, and M. A. Güler. 2021. Crashworthiness optimization of hierarchial hexagonal honeycombs under out-of-plane impact. *Proceedings of the Institution of Mechanical Engineers, Part C: Journal of Mechanical Engineering Science* 235 (6):963–74. doi:10.1177/0954406220939104.

Bernard, M. 1977. Investigation of an aluminum rolling helix crash energy absorber. Final Report no. ADA042084, ARA, Inc., West Covina, CA.

Christman, D. R. W. M. Isabell, S. G. Babcock, A. R. McMillan, and S. J. Green. 1977. *Measurements of dynamic properties of materials 6061-T6*. Technical Report no. AD 735966, General Motors Corporation, Detroit, MI.

Fragoso-Medina, O., and F. Velázquez-Villegas. 2021. Aluminum foam to improve crash safety performance: A numerical simulation approach for the automotive industry. *Mechanics Based Design of Structures and Machines* 1–15. doi:10.1080/15397734.2021.1927076.

Gao, D., and C. Zhang. 2018. Theoretical and numerical investigation on in-plane impact performance of chiral honeycomb core structure. *Journal of Structural Integrity and Maintenance* 3 (2):95–105. doi:10.1080/24705314.2018.1461772.

Gao, F. L., Y. C. Bai, C. Lin, and I. Y. Kim. 2019. A time-space kriging-based sequential metamodeling approach for multi-objective crashworthiness optimization. *Applied Mathematical Modelling* 69:378–404. doi:10.1016/j.apm.2018.12.011.

Gao, Q., C. Ge, W. Zhuang, L. Wang, and Z. Ma. 2019. Crashworthiness analysis of double-arrowed auxetic structure under axial impact loading. *Materials and Design* 161:22–34. doi:10.1016/j.matdes.2018.11.013.

Gao, Q., X. Zhao, C. Wang, L. Wang, and Z. Ma. 2018. Multi-objective crashworthiness optimization for an auxetic cylindrical structure under axial impact loading. *Materials and Design* 143:120–30. doi:10.1016/j.matdes.2018.01.063.

Guo, Y., J. Zhang, L. Chen, B. Du, H. Liu, L. Chen, W. Li, and Y. Liu. 2020. Deformation behaviors and energy absorption of auxetic lattice cylindrical structures under axial crushing load. *Aerospace Science and Technology* 98:105662. doi:10.1016/j.ast.2019.105662.

Han, M. S., B. S. Min, and J. U. Cho. 2014. Fracture properties of aluminum foam crash box. *International Journal of Automotive Technology* 15 (6):945–51. doi:10.1007/s12239-014-0099-2.

Hou, S., W. Tan, Y. Zheng, X. Han, and Q. Li. 2014. Optimization design of corrugated beam guardrail based on RBF-MQ surrogate model and collision safety consideration. *Advances in Engineering Software* 78:28–40. doi:10.1016/j.advengsoft.2014.08.002.

Hou, X., Z. Deng, and K. Zhang. 2016. Dynamic crushing strength analysis of auxetic honeycombs. *Acta Mechanica Solida Sinica* 29 (5):490–501. doi:10.1016/S0894-9166(16)30267-1.

Isabell, W. M, and D. R. Christman. 1970. *Shock propagation and fracture in 6061-T6 aluminum from wave profile measurements*. Technical Report no. AD 705536, General Motors Corporation, Detroit, MI.

Jones, D. R., M. Schonlau, and W. J. Welch. 1998. Efficient global optimization of expensive black-box functions. *Journal of Global Optimization* 13 (4):455–92. doi:10.1023/A:1008306431147.

Lakes, R. 1993. Materials with structural hierarchy. *Nature* 361 (6412):511–5. doi:10.1038/361511a0.

Lee, W., Y. Jeong, J. Yoo, H. Huh, S. J. Park, S. H. Park, and J. Yoon. 2019. Effect of auxetic structures on crash behavior of cylindrical tube. *Composite Structures* 208:836–46. doi:10.1016/j.compstruct.2018.10.068.

Li, M., X. Lu, X. Zhu, X. Su, and T. Wu. 2019. Research on in-plane quasi-static mechanical properties of gradient tetra-chiral hyper-structures. *Advance Engineering Materials* 21 (3):1801038. doi:10.1002/adem.201801038.

Liu, Y., and X. C. Zhang. 2009. The influence of cell micro-topology on the in-plane dynamic crushing of honeycombs. *International Journal of Impact Engineering* 36 (1):98–109. doi:10.1016/j.ijimpeng.2008.03.001.

LS-DYNA Support. Accessed December 05, 2021. https://www.dynasupport.com/howtos/material/fromengineering-to-true-strain-true-stress.

Lu, H., X. Wang, and T. Chen. 2021. In-plane dynamics crushing of a combined auxetic honeycomb with negative Poisson's ratio and enhanced energy absorption. *Thin-Walled Structures* 160:107366. doi:10.1016/j.tws.2020.107366.

Ma, C., H. Lei, J. Hua, Y. Bai, J. Liang, and D. Fang. 2018. Experimental and simulation investigation of the reversible bi-directional twisting response of tetra-chiral cylindrical shells. *Composite Structures* 203:142–52. doi:10.1016/j.compstruct.2018.07.013.

Ma, C., H. S. Lei, J. Liang, W. W. Wu, T. J. Wang, and D. N. Fang. 2018. Macroscopic mechanical response of chiral-type cylindrical metastructures under axial compression loading. *Materials and Design* 158:198–212. doi:10.1016/j.matdes.2018.08.022.

Nia, A. A., and J. H. Hamedani. 2010. Comparative analysis of energy absorption and deformations of thin walled tubes with various section geometries. *Thin-Walled Structures* 48 (12):946–54. doi:10.1016/j.tws.2010.07.003.

Niutta, C. B., E. J. Wehrle, F. Duddeck, and G. Belingardi. 2018. Surrogate modeling in design optimization of structures with discontinuous responses. *Structural and Multidisciplinary Optimization* 57 (5):1857–69. doi:10.1007/s00158-018-1958-7.

Prall, D., and R. S. Lakes. 1997. Properties of a chiral honeycomb with a Poisson's ratio of -1. *International Journal of Mechanical Sciences* 39 (3):305–14. doi:10.1016/S0020-7403(96)00025-2.

Qi, C., A. Remennikov, L. Pei, S. Yang, Z. Yu, and T. D. Ngo. 2017. Impact and close-in blast response of auxetic honeycomb-cored sandwich panels: Experimental tests and numerical simulations. *Composite Structures* 180: 161–78. doi:10.1016/j.compstruct.2017.08.020.

Qi, C., F. Jiang, C. Yu, and S. Yang. 2019. In plane crushing response of tetra-chiral honeycombs. *International Journal of Impact Engineering* 130:247–65. doi:10.1016/j.ijimpeng.2019.04.019.

Raponi, E., M. Bujny, M. Olhofer, N. Aulig, S. Boria, and F. Duddeck. 2019. Kriging-assisted topology optimization of crash structures. *Computer Methods in Applied Mechanics and Engineering* 348:730–52. doi:10.1016/j.cma.2019.02.002.

Saenz-Dominguez, I., I. Tena, A. Esnaola, M. Sarrionandia, J. Torre, and J. Aurrekoetxea. 2019. Design and characterisation of cellular composite structures for automotive crash-boxes manufactured by out of die ultraviolet cured pultrusion. *Composites Part B: Engineering* 160:217–24. doi:10.1016/j.compositesb.2018.10.046.

Samer, F., H. Samaka, and K. S. Khalid. 2013. Improvement of energy absorption of thin walled hexagonal tube made of magnesium alloy by using trigger mechanism. *International Journal of Research in Engineering and Technology* 02 (10):173–80. doi:10.15623/ijret.2013.0210025.

Sgobba, F. 2018. Optimization of chiral cellular topologies for energy absorption. MS thesis, Politecnico Di Milano, Faculty of Industrial Engineering,

Wang, Y., J. Feng, J. Wu, and D. Hu. 2016. Effects of fiber orientation and wall thickness on energy absorption characteristics of carbon-reinforced composite tubes under different loading conditions. *Composite Structures* 153 (10):356–68. doi:10.1016/j.compstruct.2016.06.033.

World Health Organization. 2018. Global status report on road safety 2018. Accessed December 05, 2021. https://www.who.int/publications/i/item/9789241565684.

Wu, Q., Y. Gao, X. Wei, D. Mousanezhad, L. Ma, A. Vaziri, and J. Xiong. 2018. Mechanical properties and failure mechanisms of sandwich panels with ultralightweight three-dimensional hierarchical lattice cores. *International Journal of Solids and Structures* 132-133:171–87. doi:10.1016/j.ijsolstr.2017.09.024.

Wu, W., L. Geng, Y. Niu, D. Qi, X. Cui, and D. Fang. 2018. Compression twist deformation of novel tetrachiral architected cylindrical tube inspired by towel gourd tendrils. *Extreme Mechanics Letters* 20:104–11. doi:10.1016/j.eml.2018.02.001.

Yang, L., O. Harrysson, H. West, and D. Cormier. 2015. Mechanical properties of 3D reentrant honeycomb auxetic structures realized via additive manufacturing. *International Journal of Solids and Structures* 69-70:475–90. doi:10.1016/j.ijsolstr.2015.05.005.

Yildiz, A. R., and K. N. Solanki. 2012. Multi-objective optimization of vehicle crashworthiness using a new particle swarm based approach. *The International Journal of Advanced Manufacturing Technology* 59 (1-4):367–76. doi:10.1007/s00170-011-3496-y.

Zhou, G., Z. D. Ma, G. Li, A. Cheng, L. Duan, and W. Zhao. 2016. Design optimization of a novel NPR crash box based on multi-objective genetic algorithm. *Structural and Multidisciplinary Optimization* 54 (3):673–84. doi:10.1007/s00158-016-1452-z.

Appendix

Data points and corresponding FEA results

Table A1 presents the data points for the tetra-chiral and reentrant crash boxes generated using the LHS method. The circumferential number of unit cells (N) is required to be a multiple of four for square crash boxes, as the number of sides for a square is four.

The calculated *SEA* and *CLE* values for the data points are given in Tables A1 and A2, where TC denotes the tetra-chiral cylindrical crash box, TS denotes the tetra-chiral square crash box, RC denotes the reentrant cylindrical crash box, and RS denotes the reentrant square crash box.

Table A1. Data points for tetra-chiral and reentrant crash boxes.

	Tetra chiral crash box (cylindrical/square)					Reentrant crash box (cylindrical/square)			
Model No.	θ (degrees)	w (mm)	t (mm)	N	Model No.	θ (degrees)	w (mm)	t (mm)	N
1	14.42	2.057	4.606	15/16	1	14.42	2.057	4.606	15/16
2	18.65	1.847	4.309	14/16	2	18.65	1.847	4.309	14/16
3	19.21	1.956	3.782	13/12	3	19.21	1.956	3.782	13/12
4	16.51	2.354	2.085	8/8	4	16.51	2.354	2.085	8/8
5	21.74	2.150	3.314	10/8	5	21.74	2.150	3.314	10/8
6	14.10	1.728	3.556	11/12	6	14.10	1.728	3.556	11/12
7	15.62	1.658	4.903	9/8	7	15.62	1.658	4.903	9/8
8	19.85	2.278	5.616	16/16	8	19.85	2.278	5.616	16/16
9	20.93	2.211	2.961	11/12	9	20.93	2.211	2.961	11/12
10	20.19	2.256	4.775	11/12	10	20.19	2.256	4.775	11/12
11	20.27	2.470	5.255	15/16	11	18.69/20.27	1.510/2.47	5.620/5.255	16/16
12	21.81	2.076	5.759	16/16	12	21.81	2.076	5.759	16/16
13	16.65	1.899	5.110	14/16	13	16.65	1.899	5.110	14/16
14	16.02	1.773	2.175	12/12	14	16.02	1.773	2.175	12/12
15	17.86	1.711	3.175	11/12	15	15.61/17.86	1.530/1.711	1.530/3.175	8/12
16	19.78	1.649	2.230	15/16	16	19.78	1.649	2.230	15/16
17	17.33	2.185	2.352	11/12	17	17.33	2.185	2.352	11/12
18	15.09	2.428	3.689	13/12	18	15.09	2.428	3.689	13/12
19	18.35	1.778	5.052	10/8	19	18.35	1.778	5.052	10/8
20	21.49	1.560	4.515	8/8	20	21.49	1.560	4.515	8/8
21	14.77	2.227	5.354	10/8	21	14.77	2.227	5.354	10/8
22	15.86	1.607	4.803	13/12	22	15.86	1.607	4.803	13/12
23	21.24	1.908	4.275	15/16	23	21.24	1.908	4.275	15/16
24	14.37	1.506	5.803	12/12	24	14.37	1.506	5.803	12/12
25	19.46	1.580	2.849	10/8	25	19.46	1.580	2.849	10/8
26	15.46	2.030	2.710	13/12	26	15.46	2.030	2.710	13/12
27	18.52	2.384	4.022	11/12	27	18.52	2.384	4.022	11/12
28	21.14	2.411	2.517	9/8	28	21.14	2.411	2.517	9/8
29	20.57	1.812	2.458	9/8	29	20.57	1.812	2.458	9/8
30	16.91	2.112	3.034	9/8	30	16.91	2.112	3.034	9/8
31	18.94	1.700	3.219	12/12	31	18.94	1.700	3.219	12/12
32	16.27	1.992	3.919	14/16	32	16.27	1.992	3.919	14/16
33	17.59	2.166	2.699	13/12	33	17.59	2.166	2.699	13/12
34	18.20	1.853	3.490	14/16	34	18.20	1.853	3.490	14/16
35	15.22	2.001	4.414	12/12	35	15.22	2.001	4.414	12/12
36	17.74	2.319	5.495	13/12	36	17.74	2.319	5.495	13/12
37	20.71	1.527	5.599	10/8	37	20.71	1.527	5.599	10/8
38	19.12	2.491	4.182	15/16	38	20.99/19.12	1.800/2.491	5.820/4.182	13/16
39	17.15	2.340	3.893	9/8	39	17.15	2.340	3.893	9/8
40	14.82	1.928	5.929	14/16	40	14.82	1.928	5.929	14/16

Table A2. FEA results for all crash boxes.

Model No	Mass (kg)	SEA (kJ/kg)	CLE	Model No	Mass (kg)	SEA (kJ/kg)	CLE	Model No	Mass (kg)	SEA (kJ/kg)	CLE	Model No	Mass (kg)	SEA (kJ/kg)	CLE
TC_1	0.194	2.413	0.359	TS_1	0.203	2.896	0.395	RC_1	0.249	4.721	0.382	RS_1	0.268	4.609	0.377
TC_2	0.141	2.211	0.411	TS_2	0.178	2.451	0.465	RC_2	0.187	5.073	0.565	RS_2	0.233	3.867	0.449
TC_3	0.131	2.115	0.442	TS_3	0.138	1.521	0.428	RC_3	0.170	4.466	0.538	RS_3	0.207	2.747	0.488
TC_4	0.065	1.057	0.322	TS_4	0.068	0.851	0.295	RC_4	0.078	1.854	0.362	RS_4	0.084	1.479	0.382
TC_5	0.134	1.344	0.476	TS_5	0.121	0.795	0.439	RC_5	0.160	2.587	0.564	RS_5	0.143	1.758	0.651
TC_6	0.114	1.073	0.291	TS_6	0.109	1.406	0.329	RC_6	0.140	2.376	0.413	RS_6	0.140	2.517	0.421
TC_7	0.102	1.060	0.337	TS_7	0.176	0.541	0.345	RC_7	0.131	2.265	0.483	RS_7	0.200	1.393	0.645
TC_8	0.264	4.191	0.532	TS_8	0.303	3.653	0.556	RC_8	0.344	5.471	0.408	RS_8	0.388	5.025	0.445
TC_9	0.118	1.757	0.485	TS_9	0.112	2.014	0.463	RC_9	0.146	2.838	0.455	RS_9	0.146	2.584	0.414
TC_10	0.187	1.708	0.423	TS_10	0.113	2.023	0.441	RC_10	0.231	4.056	0.587	RS_10	0.265	3.364	0.507
TC_11	0.262	4.165	0.558	TS_11	0.296	3.689	0.527	RC_11	0.247	4.424	0.505	RS_11	0.383	5.275	0.431
TC_12	0.258	3.505	0.538	TS_12	0.298	3.187	0.594	RC_12	0.332	4.471	0.402	RS_12	0.378	4.684	0.509
TC_13	0.165	2.242	0.363	TS_13	0.226	2.522	0.422	RC_13	0.221	5.772	0.556	RS_13	0.291	4.097	0.420
TC_14	0.071	1.375	0.358	TS_14	0.096	0.910	0.320	RC_14	0.089	2.200	0.353	RS_14	0.114	1.288	0.321
TC_15	0.105	1.049	0.358	TS_15	0.096	1.363	0.356	RC_15	0.071	1.385	0.470	RS_15	0.123	2.259	0.456
TC_16	0.088	1.819	0.481	TS_16	0.096	1.609	0.471	RC_16	0.110	2.638	0.406	RS_16	0.120	1.820	0.329
TC_17	0.091	1.630	0.403	TS_17	0.119	1.279	0.368	RC_17	0.113	1.881	0.278	RS_17	0.142	1.615	0.298
TC_18	0.145	2.859	0.390	TS_18	0.151	2.077	0.361	RC_18	0.193	4.330	0.341	RS_18	0.197	3.381	0.359
TC_19	0.176	0.948	0.365	TS_19	0.192	0.583	0.382	RC_19	0.208	2.174	0.542	RS_19	0.218	1.238	0.589
TC_20	0.105	0.706	0.441	TS_20	0.157	0.465	0.439	RC_20	0.126	1.424	0.622	RS_20	0.177	1.043	0.669
TC_21	0.204	1.287	0.300	TS_21	0.225	0.822	0.304	RC_21	0.247	3.611	0.518	RS_21	0.261	2.249	0.580
TC_22	0.136	1.509	0.357	TS_22	0.164	1.196	0.363	RC_22	0.176	3.431	0.473	RS_22	0.201	2.408	0.502
TC_23	0.183	2.317	0.478	TS_23	0.186	2.691	0.521	RC_23	0.230	4.215	0.487	RS_23	0.242	3.531	0.424
TC_24	0.158	1.134	0.307	TS_24	0.208	1.090	0.332	RC_24	0.198	2.816	0.476	RS_24	0.250	2.157	0.491
TC_25	0.097	0.752	0.381	TS_25	0.082	0.490	0.386	RC_25	0.113	1.606	0.553	RS_25	0.095	1.070	0.639
TC_26	0.094	2.089	0.382	TS_26	0.133	1.145	0.321	RC_26	0.124	3.004	0.315	RS_26	0.116	2.538	0.336
TC_27	0.162	1.856	0.408	TS_27	0.173	2.007	0.380	RC_27	0.202	4.548	0.572	RS_27	0.221	3.394	0.434
TC_28	0.077	1.730	0.503	TS_28	0.091	0.948	0.426	RC_28	0.100	2.781	0.487	RS_28	0.110	1.635	0.520
TC_29	0.060	1.137	0.475	TS_29	0.073	0.614	0.409	RC_29	0.076	1.790	0.462	RS_29	0.087	1.320	0.649
TC_30	0.080	1.369	0.369	TS_30	0.103	0.780	0.335	RC_30	0.103	1.824	0.384	RS_30	0.123	1.794	0.578
TC_31	0.103	1.379	0.423	TS_31	0.099	1.359	0.381	RC_31	0.129	2.954	0.539	RS_31	0.126	2.260	0.485
TC_32	0.134	2.381	0.368	TS_32	0.162	2.690	0.387	RC_32	0.179	5.351	0.481	RS_32	0.217	3.433	0.315
TC_33	0.101	2.551	0.460	TS_33	0.094	1.847	0.360	RC_33	0.132	3.106	0.327	RS_33	0.125	2.353	0.328
TC_34	0.115	2.221	0.412	TS_34	0.174	1.936	0.432	RC_34	0.153	3.576	0.395	RS_34	0.215	2.912	0.398
TC_35	0.150	1.654	0.410	TS_35	0.167	1.587	0.343	RC_35	0.192	4.707	0.543	RS_35	0.211	2.871	0.407
TC_36	0.210	2.658	0.455	TS_36	0.257	1.893	0.391	RC_36	0.275	6.759	0.590	RS_36	0.318	3.532	0.457
TC_37	0.182	0.800	0.419	TS_37	0.213	0.423	0.426	RC_37	0.212	1.650	0.572	RS_37	0.237	1.065	0.730
TC_38	0.210	4.209	0.562	TS_38	0.262	3.611	0.551	RC_38	0.241	3.970	0.577	RS_38	0.292	5.196	0.401
TC_39	0.110	1.628	0.390	TS_39	0.151	0.885	0.337	RC_39	0.143	3.962	0.573	RS_39	0.180	2.195	0.594
TC_40	0.188	2.229	0.322	TS_40	0.276	2.533	0.374	RC_40	0.253	5.977	0.514	RS_40	0.352	4.592	0.427